UNSTRUCTURED NONLINEAR FREE SURFACE FLOW SOLUTIONS: VALIDATION AND VERIFICATION

Clarence O. E. Burg*, Kidambi Sreenivas*, Daniel G. Hyams* and Brent Mitchell†
Computational Simulation and Design Center
Mississippi State University
Mississippi State, Mississippi 39762 U.S.A.

Abstract

A nonlinear free surface solution methodology is incorporated within an existing three-dimensional, unstructured Navier-Stokes solver, U^2NCLE. This portable, parallel solver uses a node-based finite volume method to solve the incompressible Reynolds-averaged Navier-Stokes equations on mixed element high-aspect ratio grids, includes several turbulence models to simulate the affects of turbulence within the boundary layer, and has the capability to simulate flow through rotating propellers accurately. To obtain a nonlinear free surface, the kinematic free surface equation is solved at each time level via a finite element implementation, valid on both triangles and quadrilaterals; after several time steps (approximately 200), the grid is moved to match the free surface elevations while conforming to the geometry. Robust grid movement is achieved by using a three-dimensional extension of Farhat's torsional spring analogy. Validation studies include a grid refinement for the free surface on a circle based on a prescribed velocity field, and of flow around a submerged NACA0012 hydrofoil. For the NACA0012 hydrofoil, for the viscous and inviscid Wigley hull and for the DTMB Model 5415 series hull, wave profiles along the hull are compared against available experimental results as well as numerical results from a more mature structured nonlinear free surface code UNCLE.

Introduction

Modeling the free surface generated by surface ships and by submerged vessels near the water surface is important for proper understanding of the flow around these vessels. In particular, the free surface changes the resistance of the vessels through the water by changing the pressure distribution and the wetted surface area. The free surface affects the location and magnitude of the vortices that originate from various locations, including the bow, appendages and propellers, which can greatly affect the performance of the propellers. The wave signatures of ships and submarines is also of importance. Surface vessels under investigation by ship designers attempt to mitigate the negative influences of the free surface interaction on cavitation, power requirements and wave signature and attempt to use the free surface to improve the performance in other ways. Because of the novelty of many of these designs, which often are not direct extensions of current designs, extensive sets of experimental data may not yet exist, and designers are more apt to rely on data from numerical simulations. Furthermore, the effects on the ship's performance caused by maneuvering through a change in direction, or through various sea states, especially in regards to sea-keeping and cavitation in littoral water are of importance in the designs and can not be readily tested by experiment.

A longterm goal of the research into numerical simulations is to develop the ability to study the performance of a full ship design, including the interactions of the various appendages, sonar domes, rudders, shafts and propellers, as the ship maneuvers in response to changes in the settings of the rudders and propellers. To accomplish this goal, efficient and accurate free surface simulations are needed. Other necessary components to achieve this goal include capabilities to monitor the onset of incipient cavitation, to perform simulation of several vessels in motion relative to one another and to adapt the grid to capture vortices in the water.

Currently, the implicit unstructured code being developed by researchers in the Computational Simulation and Design Center at Mississippi State University solves the three-dimensional, turbulent, incompressible Navier-Stokes equations, via an edge-based, flux-differencing finite volume methodology with Roe-averaged variables. Hyams[1] successfully parallelized

* Assistant Research Professor, Member AIAA
† Research Associate

the code and has ported the code to a wide variety of high performance machines. The unstructured grid generator[2] has the capability of building highly stretched high-aspect ratio grids near viscous surfaces, which include higher order elements such as pyramids and prisms. Other areas of code development include realistic rudder and propeller-induced motion and full-scale Reynolds number simulation.

Much of this work is an extrapolation of the free surface algorithm used within the three-dimensional structured code UNCLE also developed at Mississippi State University. Beddhu[3] developed the structured free surface solver, using a modified artificial compressibility formulation. This algorithm was applied to steady and unsteady flow around the Wigley hull[4], to the nonappended DTMB model 5415 series hull[5], to the Series 60 $C_B = 0.6$ ship[6] and to a more detailed stern analysis for the model 5415 series hull[7], which were presented at the Gothenburg 2000 conference[8].

Navier-Stokes Solution Algorithm

Three different sets of equations are solved in the process of simulating the flow around surface ships and submerged vessels near the water surface. The unsteady incompressible Reynolds-averaged Navier-Stokes equations, which are presented here in Cartesian coordinates and in conservative form, are solved to determine the velocity and pressure within the computational domain. Either the Spalart-Allmaras[9] or the $q-\omega$ turbulence model[10] is used to simulate the turbulent viscosity primarily within the boundary layer, and the kinematic free surface equation is solved to advance the free surface in time.

Assuming that gravity acts in the y-direction (i.e., the vertical direction), the incompressible Navier-Stokes equations can be expressed in dimensional form, denoted with superscript *, as

$$\frac{\partial u^*}{\partial x^*} + \frac{\partial v^*}{\partial y^*} + \frac{\partial w^*}{\partial z^*} = 0$$

$$\frac{\partial u^*}{\partial t^*} + \frac{\partial}{\partial x^*}\left(u^{*2} + \frac{P^*}{\rho_\infty}\right) + \frac{\partial}{\partial y^*}\left(u^* v^*\right) + \frac{\partial}{\partial z^*}\left(u^* w^*\right) = \mu^* \nabla^2 u^*$$

$$\frac{\partial v^*}{\partial t^*} + \frac{\partial}{\partial x^*}\left(u^* v^*\right) + \frac{\partial}{\partial y^*}\left(v^{*2} + \frac{P^*}{\rho_\infty} + g y^*\right) + \frac{\partial}{\partial z^*}\left(v^* w^*\right) = \mu^* \nabla^2 v^*$$

$$\frac{\partial w^*}{\partial t^*} + \frac{\partial}{\partial x^*}\left(u^* w^*\right) + \frac{\partial}{\partial y^*}\left(v^* w^*\right) + \frac{\partial}{\partial z^*}\left(w^{*2} + \frac{P^*}{\rho_\infty}\right) = \mu^* \nabla^2 w^* \quad (1)$$

The variables in the preceding equation are normalized with respect to a characteristic length scale (L) and free stream values of velocity (U_∞), density (ρ_∞), and viscosity (μ_∞). Thus, the Reynolds number is defined as $Re = U_\infty L/\nu_\infty$. Pressure is normalized with $P = (P^* + \rho_\infty g y^* - P_\infty)/\rho_\infty U_\infty^2$, where P^* is the local dimensional static pressure. Following Chorin[11] and Taylor[12], an artificial time derivative term ($\partial \rho_a / \partial t$, where $\rho_a = P/\beta$) has been added to the continuity equation to cast the complete set of governing equations into a time-marching form. The nondimensionalized equations can be written in integral form as

$$\frac{\partial}{\partial t}\int_\Omega Q d\mathcal{V} + \int_{\partial\Omega} \vec{F}\cdot\hat{\vec{n}} dA = \frac{1}{Re}\int_{\partial\Omega} \vec{G}\cdot\hat{\vec{n}} dA \quad (2)$$

where $\hat{\vec{n}}$ is the outward pointing unit normal to the control volume $\mathcal{V}$. The vector of dependent variables and the components of the inviscid and viscous flux vectors are given as

$$Q = \begin{bmatrix} P \\ u \\ v \\ w \end{bmatrix} \quad (3)$$

$$F\cdot\hat{\vec{n}} = \begin{bmatrix} \beta(\Theta - a_t) \\ u\Theta + \hat{n}_x P \\ v\Theta + \hat{n}_y P \\ w\Theta + \hat{n}_z P \end{bmatrix} \quad (4)$$

$$G\cdot\hat{\vec{n}} = \begin{bmatrix} 0 \\ \hat{n}_x\tau_{xx} + \hat{n}_y\tau_{xy} + \hat{n}_z\tau_{xz} \\ \hat{n}_x\tau_{yx} + \hat{n}_y\tau_{yy} + \hat{n}_z\tau_{yz} \\ \hat{n}_x\tau_{zx} + \hat{n}_y\tau_{zy} + \hat{n}_z\tau_{zz} \end{bmatrix} \quad (5)$$

where β is the artificial compressibility parameter (typically 15 in this work), u, v, and w are the Cartesian velocity components in the x, y, and z directions, and $\hat{n}_x$, $\hat{n}_y$, and $\hat{n}_z$ are the components of the normalized control volume face vector. Θ is the velocity normal to a control volume face:

$$\Theta = \hat{n}_x u + \hat{n}_y v + \hat{n}_z w + a_t \quad (6)$$

where the grid speed $a_t = -(V_x\hat{n}_x + V_y\hat{n}_y + V_z\hat{n}_z)$. Note that $\vec{V}_s = V_x\hat{i} + V_y\hat{j} + V_z\hat{k}$ is the control volume face velocity. The viscous stresses given in Equation 5 are

$$\tau_{ij} = (\mu + \mu_t)\left(\frac{\partial u_i}{\partial x_j} + \frac{\partial u_j}{\partial x_i}\right) \quad (7)$$

where μ and μ_t are the molecular and eddy viscosities, respectively.

The incompressible Reynolds-averaged Navier-Stokes equations are discretized via an edge-based, node-centered finite volume methodology using Roe-averaged variables to calculate the flux across the control volume faces and a directional derivative approach and a least squares method to integrate the viscous terms. Once discretized, the equations are solved implicitly using a symmetric Gauss-Seidel solver. For a better understanding of the flow solver, the interested reader is directed to Hyams[13,14].

Nonlinear Free Surface Algorithm

A nonlinear free surface is obtained for a steady-state simulation by solving the kinematic free surface boundary condition at each time level and imposing the hydrostatic pressure distribution based on the new free surface elevation onto the free surface boundary within the mean flow. After several time steps, typically on the order of 200, the grid is moved to match the free surface elevations while conforming to the surfaces that intersect the free surface, such as the hull of a ship or the sail of a submarine; and as the loosely coupled interaction between the free surface solver, the RANS solver and the grid movement algorithm converges, the solution converges to the nonlinear free surface solution.

In deriving the kinematic free surface boundary condition, the free surface $\eta(x, y, z, t) = 0$ is considered as a material surface (i.e., no flow travels through the surface), so

$$\frac{D\eta}{Dt} = 0 \tag{8}$$

or

$$\frac{\partial \eta}{\partial t} + (u - V_x)\frac{\partial \eta}{\partial x} + (v - V_y)\frac{\partial \eta}{\partial y} + (w - V_z)\frac{\partial \eta}{\partial z} = 0 \tag{9}$$

By making the assumption that the free surface η can be expressed as $\eta(x, y, z, t) = y - Y(x, z, t) = 0$, this equation reduces to

$$\frac{\partial Y}{\partial t} + (u - V_x)\frac{\partial Y}{\partial x} - (v - V_y) + (w - V_z)\frac{\partial Y}{\partial z} = 0 \tag{10}$$

At steady-state, the kinematic boundary condition becomes

$$\begin{aligned} (\vec{u} + a_t) \cdot \left(\frac{\partial Y}{\partial x}, -1, \frac{\partial Y}{\partial z} \right) &= 0 \\ (\vec{u} + a_t) \cdot \alpha \hat{n}_{fs} &= 0 \end{aligned} \tag{11}$$

where $\alpha = \sqrt{1 + \left(\frac{\partial Y}{\partial x}\right)^2 + \left(\frac{\partial Y}{\partial z}\right)^2}$ and a_t is the grid speed $-(V_x \hat{n}_x + V_y \hat{n}_y + V_z \hat{n}_z)$, so the flow is tangent to the free surface at steady-state.

The pressure in the numerical simulation at the free surface is set based on the free surface elevation. For the original, dimensional equations, the pressure at the free surface is the atmospheric pressure P_∞. Using the nondimensionalization, $P = \frac{P^* + \rho_\infty g y^* - P_\infty}{\rho_\infty U_\infty^2}$ with $P^* = P_\infty$ and $\frac{y^*}{L} = Y$, the pressure is set to $P = \frac{Y}{Fr^2}$, where the Froude number is $\frac{U_\infty}{\sqrt{gL}}$.

Free Surface Solution Algorithm

The kinematic equation for the linear free surface is solved via a Galerkin finite element approach. In this approach, an algebraic equation is obtained for each node j by multiplying the governing equation by a weight function $\varphi_j(x, z)$, approximating the terms in the governing equation by using linear and bilinear interpolating functions $\phi_i(x, z)$ and integrating over the computational domain, or

$$\int_\Omega \varphi_j(x,z) \left(\frac{\partial \tilde{Y}}{\partial t} + \left(\tilde{u} - \tilde{V}_x\right)\frac{\partial \tilde{Y}}{\partial x} - \left(\tilde{v} - \tilde{V}_y\right) + \left(\tilde{w} - \tilde{V}_z\right)\frac{\partial \tilde{Y}}{\partial z} \right) = 0 \tag{12}$$

where $\tilde{Y}(x, z) = \sum_i Y_i \phi_i(x, z)$ is the interpolated free surface elevation and $\tilde{u}(x, z) = \sum_i u_i \phi_i(x, z)$ is the u-velocity, with the other velocity components of a similar form.

For the triangular elements, the resulting equations are integrated using 7 point Gauss quadrature, and for the quadrilateral elements, the integrals are solved either using 6 point Gauss quadrature in both directions. A first-order backward time discretization of Equation 12 is used for the temporal derivative, where $\frac{\partial \tilde{Y}}{\partial t} = \frac{\tilde{Y}^{n+1} - \tilde{Y}^n}{\Delta t}$ and the spatial terms are evaluated at the unknown time level $n + 1$. This discretization results in a linear algebraic system of the form $\Re_{fs}(Y^{n+1}, Y^n) = 0$. Since these equations are linear in the unknown variable Y_i^{n+1} at each time level (i.e., the velocities are frozen), the Jacobian matrix is calculated only once per time level. A Gauss-Seidel iterative solver is used to identify the solution of the kinematic free surface equation by solving

$$\left[\frac{\partial \Re_{fs}}{\partial Y^{n+1}}\right] \Delta y^{n+1,m} = -\Re_{fs}(Y^{n+1,m}, Y^n) \tag{13}$$

where $Y^{n+1,m+1} = Y^{n+1,m} + \Delta y^{n+1,m}$ and $Y^{n+1} = Y^{n+1,m+1}$ when $\|\Delta y^{n+1,m}\| <$ tolerance.

Within the viscous boundary layer, special care is needed in solving the kinematic free surface equation. On viscous surfaces, the flow velocity plus the grid velocity (i.e., $\vec{u} + a_t$) is set to zero, which prevents the free surface from moving at the viscous surface. Physically, however, the effects of surface tension force the free surface to rise and fall along the viscous surfaces. Since the solver does not simulate surface tension, another method must be employed to move the free surface near the viscous surfaces. Following the method used in the structured solver, the free surface at a certain distance from the viscous surface is extended at a constant height to the viscous surface. This distance is typically on the order of 2×10^{-4} times the characteristic length L, whereas the point spacing off of the viscous surface is on the order 10^{-6} for model scale simulations and 10^{-8} for full scale simulations.

Free Surface Boundary Condition

At the free surface boundary, the pressure is set to the hydrostatic pressure of $P = \frac{Y}{Fr^2}$. Determining the velocity to impose on the boundary is more difficult. If the velocity were forced to be tangent to the free surface (i.e., $(\vec{u} + a_t) \cdot \hat{n}_{fs} = 0$), then the free surface equation would reduce to $\frac{\partial Y}{\partial t} = 0$, and the free surface could not evolve. Thus, this tangency condition is relaxed to allow the free surface to evolve.

This boundary condition is implemented using a characteristic variable boundary condition, similar to the derivation used for the farfield boundary condition. For hyperbolic systems, flow information travels along characteristics; and for the equations of interest, three characteristics originate upstream, and one originates downstream. If the flow is traveling out of the domain (i.e, $(\vec{u} + a_t) \cdot \hat{n} > 0$), then only one characteristic needs to be specified from the outside, which is derived from the hydrostatic pressure. If the flow is traveling into the domain, three characteristics need to be specified from the outside.

The characteristic variables are derived from considering the inviscid fluxes across the the boundary face, via

$$\frac{\partial Q}{\partial t} + \nabla F \cdot \hat{\vec{n}} = 0 \tag{14}$$

where $\hat{\vec{n}}$ is the normal to the grid for each boundary face. The inviscid flux term can be rewritten as

$$\nabla F = \frac{\partial F}{\partial Q} \nabla Q = R \Lambda R^{-1} \nabla Q \tag{15}$$

where Λ is a diagonal matrix with the eigenvalues Θ, Θ, $\Theta + c$ and $\Theta - c$, where $\Theta = u\hat{n}_x + v\hat{n}_y + w\hat{n}_z + a_t$ and $c = \sqrt{\left(\Theta - \frac{a_t}{2}\right)^2 + \beta}$. Premultiplying by R^{-1},

$$R^{-1} \frac{\partial Q}{\partial t} + \Lambda R^{-1} \nabla Q \cdot \hat{\vec{n}} = 0 \tag{16}$$

Freezing the matrix $R_o^{-1} = R^{-1}(Q^{in})$,

$$\frac{\partial R_o^{-1} Q}{\partial t} + \Lambda \nabla \left(R_o^{-1} Q\right) \cdot \hat{\vec{n}} = 0 \tag{17}$$

Using the definition $W(Q) = R_o^{-1} Q$, Equation 14 decouples into four equations for the four characteristic variables W as

$$\frac{\partial W}{\partial t} + \Lambda \nabla W \cdot \hat{\vec{n}} = 0 \tag{18}$$

Three of the characteristics are obtained from upstream values, and one of the characteristics is obtained from downstream values. In the case of a boundary face, there are a set of characteristics associated with the inside flow $W^{in}(Q^{in})$ and a set of characteristics associated with the outside flow $W^{out}(Q^{out})$. The flow variables on the boundary face are determined from the appropriate characteristic variables via $Q = R_o W$. For flow traveling out of the domain, the characteristic variables are chosen to be

$$W = \begin{bmatrix} w_1^{in} \\ w_2^{in} \\ w_3^{in} \\ w_4^{out} \end{bmatrix} \tag{19}$$

because the fourth eigenvalue $\Theta - c$ is negative, while the other eigenvalues are positive. For flow traveling into the domain, only the third eigenvalue is positive, so the characteristic variables are chosen as

$$W = \begin{bmatrix} w_1^{out} \\ w_2^{out} \\ w_3^{in} \\ w_4^{out} \end{bmatrix} \tag{20}$$

For farfield boundary conditions, the characteristic variables associated with the outside flow are taken as the free stream variables. For free surface boundary conditions, the characteristic variables for the outside flow are determined from the hydrostatic pressure and the only available velocity information, which is the velocity on the inside. However, this velocity is modified by removing a portion of the velocity component that is not tangent to the grid, via

$$\vec{u}^{out} = (\vec{u} + a_t) - \gamma \left((\vec{u} + a_t) \cdot \hat{n}\right) (\vec{u} + a_t) \tag{21}$$

where

$$\gamma = \begin{cases} -(\vec{u} + a_t) \cdot \hat{n} & \text{if} \quad -1 \leq (\vec{u} + a_t) \cdot \hat{n} < 0 \\ 1 & \text{if} \quad (\vec{u} + a_t) \cdot \hat{n} < -1 \end{cases} \tag{22}$$

When γ is 1, the velocity imposed from the outside is tangent to the grid (i.e., $\left(\vec{u^{out}} + a_t\right) \cdot \hat{n} = 0$). When the velocity was not modified or constrained in some fashion, the free surface algorithm became unstable for flow into the domain due to the inconsistency of using downstream information. This modification provides enough control over the velocity to maintain stability of the algorithm, and if the grid is allowed to move to match the free surface, then this modification ensures that the flow will be tangent to the free surface at convergence.

Grid Movement Algorithm

After several time steps, the grid is moved to match the free surface while conforming to any solid surfaces intersecting the free surface, with displacements on the surface being propagated into the volume grid. Several methods are available for this grid movement, including the use of a Laplacian solver to propagate the surface perturbations into the volume grid, the use of a linear spring analogy where each edge is a spring whose stiffness is determined by the length of the edge, a torsional/linear spring analogy where the angle between the edges affects the stiffness of the springs in the mesh, or solving the linear elasticity equations to propagate the perturbations within the grid. The spring analogy is computationally efficient but is not robust. Both the spring analogy and the Laplacian solver generate elements with negative volumes for moderate amounts of movement, on the order of the size of 3 to 4 elements. Solving the linear elasticity equations to move the grid is robust, but the computational cost associated with this method is the primary drawback.

Thus, following the work of Farhat[15] and extending it to three dimensional grids, the torsional/linear spring analogy has been developed and applied to the problem of moving the grid to match the linear free surface elevations. For tetrahedral grids, this method is quite robust, allowing severe distortions on the surface while maintaining positive volume elements. In practice, this algorithm allows up to approximately 80% compression of elements. Within the boundary layer, (i.e., near the viscous surfaces), the grid moves rigidly in relation to the points on the boundary. This grid movement method is computationally costly but provides excellent robustness for the free surface solver.

The linear spring method for moving an unstructured grid is presented by Batina[16] where each edge in the grid is replaced by a linear spring whose stiffness is inversely proportional to the length of the edge. Thus, for the edge connecting nodes i and j, the stiffness k_{ij} of the spring is

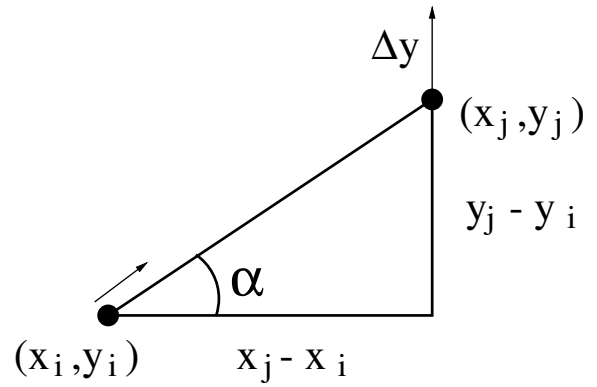

Figure 1: A Displacement in y-Direction Results in Displacements in x and y Directions

$$k_{ij} = \frac{1}{((x_i - x_j)^2 + (y_i - y_j)^2)^{p/2}} = \frac{1}{l_{ij}^p} \tag{23}$$

where the coordinates of nodes i and j are (x_i, y_i) and (x_j, y_j) and p is a predetermined coefficient, usually 1 or 2, and $l_{ij} = \sqrt{((x_i - x_j)^2 + (y_i - y_j)^2)}$. Given a set of nodal displacements or forces acting on the boundary of the computational grid, the following equations for the interior displacements are solved iteratively until all the forces are in equilibrium

$$\begin{aligned} \Delta x_j^{n+1} &= \frac{\sum_i k_{ij} \Delta x_i^n}{\sum_i k_{ij}} \\ \Delta y_j^{n+1} &= \frac{\sum_i k_{ij} \Delta y_i^n}{\sum_i k_{ij}} \end{aligned} \tag{24}$$

where i is summed over all edges connected to node j. This method is easily extended to three dimensions and is computationally efficient requiring only a few Jacobi iterations to achieve an acceptable level of accuracy. Several researchers have used this method to move nodes in unstructured grids for simulating flows around objects in relative motion[17] and for design optimization[18].

Technically speaking, these equations do not simulate the behavior of a network of springs because there is no interaction between the x and y coordinates. A displacement in one coordinate will not influence the location in the other coordinate, as would be the case for

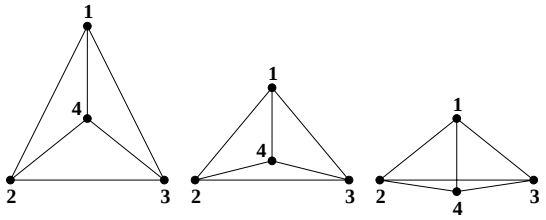

Figure 2: Negative Areas Produced by Linear Spring Method

a network of springs. An example of this coupled interplay is shown in Figure 1, where a displacement in the y-direction is applied to node j which results in a displacement in both directions for node i. To simulate the behavior of a network of springs, the following set of equations for each spring must be summed over all springs:

forces in the x-direction :

$$k_{ij}\left[(\Delta x_i - \Delta x_j)\cos^2\alpha + (\Delta y_i - \Delta y_j)\cos\alpha\sin\alpha\right] \quad (25)$$

forces in the y-direction :

$$k_{ij}\left[(\Delta x_i - \Delta x_j)\cos\alpha\sin\alpha + (\Delta y_i - \Delta y_j)\sin^2\alpha\right]$$

Unfortunately, this method often fails for complicated geometries and for large changes in the boundary, because negative areas are generated when a node crosses over an edge in the grid. The creation of negative areas is illustrated in Figure 2, where node 1 is pushed downwards and node 4 is forced to cross the edge between nodes 2 and 3. The reason for this failure is that the stiffness in the linear spring method prevents two nodes from colliding but does not prevent a node from crossing over an edge. As two nodes get closer together, the stiffness increases without bound preventing the collision; but there is no mechanism to prevent a node from crossing an edge, because these crossovers can occur without the stiffness increasing without bound.

To provide a more robust movement algorithm for unstructured grid, Farhat developed an algorithm to prevent a node from crossing an edge by using torsional springs around each node, as shown in Figure 3. The stiffness of the torsion spring C_{ijk} is inversely proportional to the sine of the angle, so that the stiffness grows without bound as the angle decreases towards zero or increases towards 180^o, or

$$C_{ijk} = \frac{1}{\sin^2\theta_i^{ijk}} \quad (26)$$

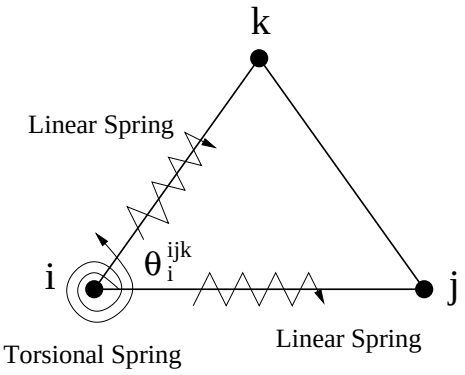

Figure 3: Placement of Linear and Torsion Springs

where θ_i^{ijk} is the angle centered at node i formed from the edges ij and ik. Thus, as a node moves towards an edge, the angle goes towards zero, and the stiffness of the torsion spring grows. The sine of the angle is squared to prevent a negative stiffness.

In Farhat[15], the equations for the torsional spring methods are derived for two-dimensional grids, and an iterative solution method is presented. In the present work, these methods have been extended into three dimensions, which provides an adequate level of robustness for the grid movement algorithm. The derivation of the three-dimensional torsional spring equations is not the focus of this paper and will be presented elsewhere.

Examples

The examples presented in this section include those that verify the implementation of the nonlinear free surface algorithm and those that validate the numerical solution from the unstructured code against experimental results and numerical results generated by the more mature and tested structured UNCLE flow solver. Code verification studies demonstrate that the implementation of the kinematic free surface equation converges quadratically to the exact solution and that the loosely coupled relationship between the Euler version of the Navier-Stokes flow solver and the free surface solver, including the grid movement algorithm, yields superlinear convergence to the continuum solution. Results from the unstructured code are compared against experimental and other numerical results for a submerged NACA0012 hydrofoil, for the Wigley hull and for the DTMB Model 5415 Series hull.

Verification

Several grid refinement studies were performed to verify that the nonlinear free surface algorithm yields

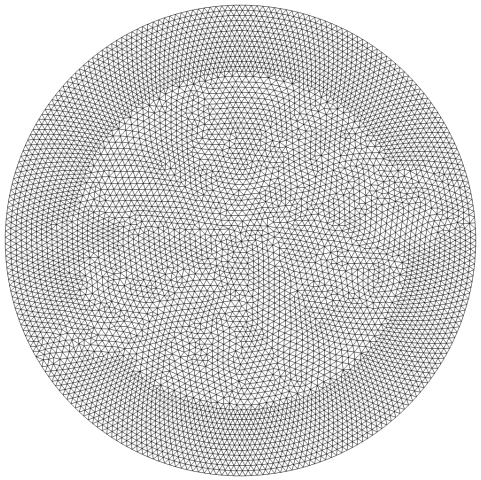

Figure 4: Circular Face for Grid 2

superlinear convergence to the continuum solution. The Galerkin finite element implementation of the kinematic free surface boundary condition yields second order convergence theoretically. To verify this result, a grid refinement study was performed on a series of cylindrical grids where only the kinematic free surface equation was solved on one of the circular faces. In this study, an exact free surface was chosen, and the velocity distribution consistent with this free surface was imposed, in order to drive the free surface towards the exact solution. Two other grid refinement studies were performed, using the NACA0012 hydrofoil, to demonstrate superlinear convergence of the free surface solver coupled with the Euler version of the flow solver with and without moving the grid to match the free surface.

Circle

The order of accuracy of the Galerkin finite element solver of the kinematic free surface equation was studied on a series of cylindrical grids, where the free surface was solved on one of the circular faces, based on an imposed velocity distribution without reference to the Navier-Stokes solver. The radius of the circle was scaled to a non-dimensional length of 1. The target free surface was

$$Y(x,z) = e^{\left(\frac{x^2+z^2}{x^2+z^2-2}\right)} \tag{27}$$

The grid velocity was set to 0, or $a_t = 0$. The velocity components u and w were chosen as

$$\begin{aligned} u(x,z) &= x \\ w(x,z) &= z \end{aligned} \tag{28}$$

Grid	Spacing on Circle	Free Surface Nodes
Grid 1	0.025	1573
Grid 2	0.0125	6080
Grid 3	0.00625	24169
Grid 4	0.003125	95911
Grid 5	0.0015625	381537

Table 1: Description of Grids for Circle Simulations

and using the kinematic free surface equation at steady state (i.e., $\frac{\partial Y}{\partial t} = 0$), the vertical velocity component v can be written as

$$v = u\frac{\partial Y}{\partial x} + w\frac{\partial Y}{\partial z} \tag{29}$$

which for this example reduces to

$$v = -2e^{\left(\frac{x^2+z^2}{x^2+z^2-2}\right)}\left(\frac{x^2+z^2}{(x^2+z^2-2)^2}\right) \tag{30}$$

The kinematic free surface equation is solved using this velocity distribution and fixing the free surface along the outer boundary of the circular face.

A series of 5 grids were used in this study and were described in Table 1, and the circular face for Grid 2 is shown in Figure 4 which demonstrates that the grid and the grid generation process were fully unstructured. As the grid spacing on the edge is reduced by a factor of 2, the number of points in the circular free surface increased by roughly a factor 4, as expected.

The error between the converged solution on each grid and the exact solution was computed via an L2-Norm as

$$E(Grid) = \sqrt{\sum_{i=1}^{\text{Nodes}} \left(Y_i^e(x,z) - Y_i^{Grid}(x,z)\right)^2 A_i} \tag{31}$$

where Y_i^e is the exact free surface at each node in the computational grid, Y_i^{Grid} is the computed free surface elevation based on the converged solution for a particular grid, and A_i is the area associated with each node in the grid. The error for each grid is presented in Table 2 and decreases from one grid to the next finer grid at a rate that is approximately quadratic. These results demonstrate that the solver of the kinematic equations has been properly implemented since it approximately achieves the theoretical order of accuracy.

NACA 0012 Hydrofoil

Researchers have used the submerged NACA0012 hydrofoil as a test case for numerical simulation, in part

Grid	Function Value	Ratio	Accuracy
Grid 1	0.00568889	N/A	N/A
Grid 2	0.00158426	3.591	1.844
Grid 3	0.00028925	5.477	2.453
Grid 4	0.00008162	3.544	1.825
Grid 5	0.00002474	3.299	1.722

Table 2: Error Results for Circle Grids

Grid	Nodes	Prisms	Free Surface Nodes
Grid 1	6999	8698	636
Grid 2	27300	35128	1275
Grid 3	104151	136322	2550
Grid 4	412941	545494	5100

Table 3: Description of Grids for NACA 0012 Hydrofoil

due to the experimental results generated by Duncan[19]. The experimental results of particular interest are for the test case with the hydrofoil at a 5 degree angle of attack. The experimental results were measured along the centerline of a tank whose dimensions was 24 m long, 61 cm deep and 61 cm wide. The hydrofoil was located at a submergence of 21.0 cm and had a length of 20.3 cm, and the flow rate was 80 cm/sec. Nondimensionalizing by the chord length of 20.3 cm, the Froude number was 0.5672 and the submergence was 1.034 L.

Hino[20] used the NACA 0012 Hydrofoil test case to validate his two-dimensional unstructured, incompressible Euler code, on a sequence of 4 grids ranging in size from 409 nodes to 6,587 nodes, with a large amount of grid packing along the free surface. The purpose of the sequence of grids was for the multigrid solver, rather than for a grid refinement study. Lohner[21] also used this test case to validate his three-dimensional unstructured, incompressible Navier-Stokes code, on a grid consisting of 465,752 points, with packing near the free surface and in the wake region behind the hydrofoil. The numerical results of Hino and Lohner were consistent with each other for the Euler versions of the codes.

Due to the relative simplicity of this geometry, it was chosen as a test case for a grid refinement study to analyze the order of accuracy of the free surface solver coupled with the Euler solver with and without the grid movement algorithm. Neither Hino nor Lohner modeled the effects of the tank boundaries, but rather assumed that the flow was purely two-dimensional. The simulations presented herein make the same assumption.

In the first grid refinement study, the grids were not allowed to move based on changes in the free surface

Grid	Error	Ratio	Accuracy
Grids 1-2	0.0031630	N/A	N/A
Grids 2-3	0.0011427	2.768	1.47
Grids 3-4	0.0003921	2.914	1.54

Table 4: Error for Linear Free Surface around NACA 0012 Hydrofoil

Grid	Error	Ratio	Accuracy
Grids 1-2	0.0039086	N/A	N/A
Grids 2-3	0.0013229	2.95	1.56
Grids 3-4	0.0004600	2.88	1.53

Table 5: Error for Nonlinear Free Surface around NACA 0012 Hydrofoil

and thus the grid along which the free surface was solved remained flat. In the second grid refinement study, the grids were moved to match the free surface. Hence, any potential degradation in the free surface algorithm due to the grid movement algorithm could be analyzed. In both refinement studies, the same base grids were employed. These grids were two-dimensional grids extruded into three dimensions by the use of prismatic elements and are described in Table 3. To avoid spurious oscillations due to farfield boundaries, the inflow and outflow boundaries were set at 30 characteristic lengths from the hydrofoil. The number of nodes in the free surface doubled each time as the grid spacing along each edge was halved; however, the number of nodes and prisms within the grid did not quadruple each time because the grid was rebuilt based on the boundary spacing rather than being created by subdividing the coarser grid. The unperturbed grid for Grid 2 in the refinement study is given in Figure 5 and the converged nonlinear free surface grid is shown in Figure 6. The grid is packed near the leading and trailing edge of the hydrofoil to capture the effects in these regions, and the interior grid near the free surface is refined due to the resolution in the free surface itself. The free surface is more refined than the interior grid so as to capture and maintain the free surface effects further downstream.

The error was calculated by comparing the converged solution between successive grids in the refinement via the following formula

$$E(Grid_i, Grid_j) = \sqrt{\int_{-2}^{2} \left(\tilde{Y}_i(x) - \tilde{Y}_j(x)\right)^2 dx} \tag{32}$$

where $\tilde{Y}_i(x)$ and $\tilde{Y}_j(x)$ are continuous functions that are

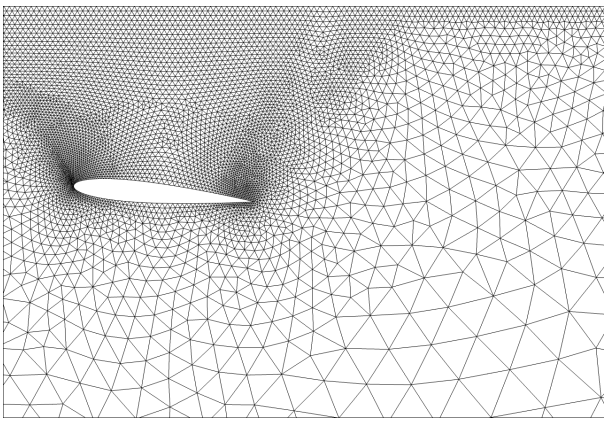

Figure 5: Side View of Original Grid 2

piecewise linear interpolations based on the free surface elevations at each node in the grid. This integral was evaluated using the trapezoid rule. The error was integrated from ahead of the hydrofoil at $x = -2$ to a location just downstream of the hydrofoil, due to the gradual phase shift in the solutions downstream of the hydrofoil. This phase shift in the wave generated by the hydrofoil can be seen in Figure 7, which shows the nonlinear free surface wave heights. The results for the grid refinement study where the grid was not moved is shown in Table 4. From this study, the order of accuracy for the free surface solver coupled with the Euler solver is better than first order accurate but is not quite second order accurate.

The results for the coupling of the free surface solver, the Euler solver and the grid movement algorithm are given in Table 5. These results seem to indicate that the grid movement algorithm does not degrade the order of accuracy of the overall free surface solver coupled with the Euler solver.

Validation

The nonlinear free surface methodology implemented within the unstructured incompressible Navier-Stokes flow solver U^2NCLE has been tested against available experimental results and a more mature structured nonlinear free surface flow solver, $UNCLE$[3,4,5,6,7,8,22]. The validation cases include a viscous and an inviscid Wigley hull simulation and a nonappended DTMB Model 5415 Series Hull. In both cases, the intersection of the free surface with the hull is presented, and for the Model 5415 Series Hull, the stern

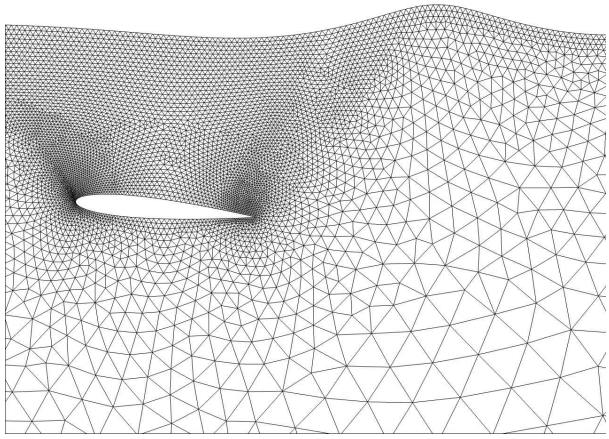

Figure 6: Side View of Converged Nonlinear Free Surface for Grid 2

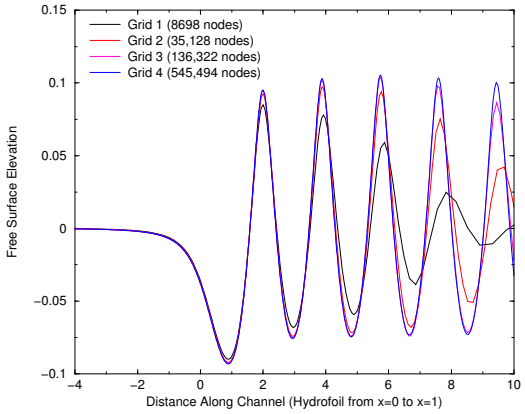

Figure 7: Nonlinear Free Surface Flow around NACA 0012 Hydrofoil

region is compared with available experimental data.

Wigley

The Wigley hull[23] is a notional hull whose shape is determined from its mathematical definition, which is given by

$$z(x,y) = \frac{B}{2}\left(1-4x^2\right)\left(1-\left(\frac{y}{D}\right)^2\right) \qquad (33)$$

where B is the maximum thickness of the hull and D is the draft of the hull, and are set to 0.1 and 0.0625 respectively. In this form, the Wigley hull is commonly used for code validation and verification. The results, given in Figure 8 and Figure 9, compare both an inviscid and a viscous unstructured simulation with the results from the viscous structured solver $UNCLE$ as well as the experimental result for a Froude number of 0.289 and a Reynolds number of 3.3 million. For the bow wave near $x = -0.45$, both the inviscid and the viscous unstructured results match the structured result nicely, while the viscous results appear to conform to the experiment results better than the inviscid results or the structured results further down the hull. In Figure 10, an overview of the free surface Kelvin wave pattern generated by the numerical simulation on an inviscid grid is compared with the experimental results. In this plot, the features of the Kelvin wave compare admirably with the experimental results, for more than a hull length downstream. This simulation was performed on a grid where the free surface grid maintained a reasonable level of resolution for several hull lengths, and the Kelvin wave pattern is adequately captured within this area of resolution. Thus, by increasing the area of resolution in the free surface grid, the wave patterns generated by the hull are probably maintainable for many hull lengths behind the ship. By increasing the resolution in the free surface grid for the NACA 0012 hydrofoil example, the wave pattern continues for at least 5 wavelengths past the hydrofoil as shown in Figure 7.

DTMB Model 5415

The most complicated example is the flow around the DTMB Model 5415 series hull, which has a transom stern and is more representative of naval ships. Experimental simulations have been run with this model at the Naval Surface Warfare Center Carderock Division[24,25], and several researchers have used this data for simulation validation purposes, particularly at the Gothenburg 2000 conference in Sweden[26].

This simulation was run at the 2.06 m/sec flow conditions, which resulted in a Froude number of 0.28 and

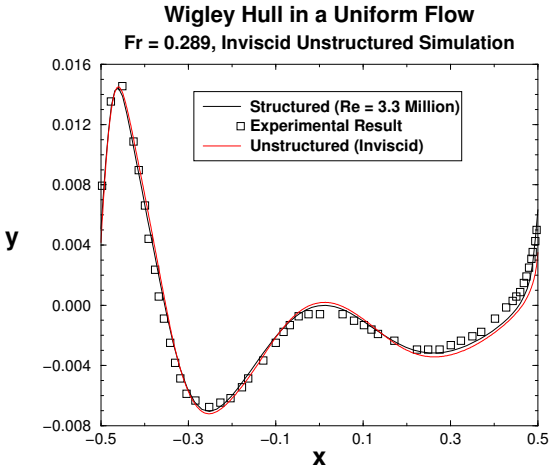

Figure 8: Inviscid Wigley Hull Profile

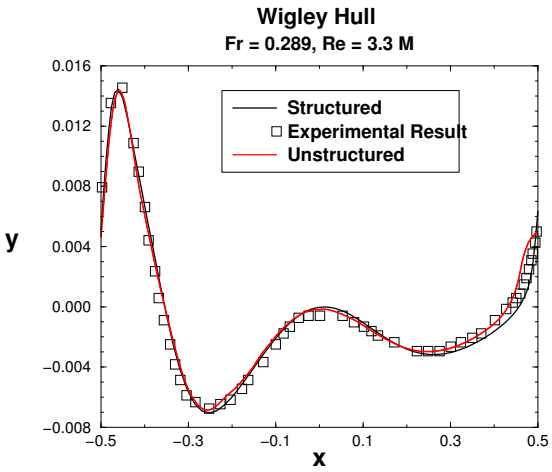

Figure 9: Viscous Wigley Hull Profile

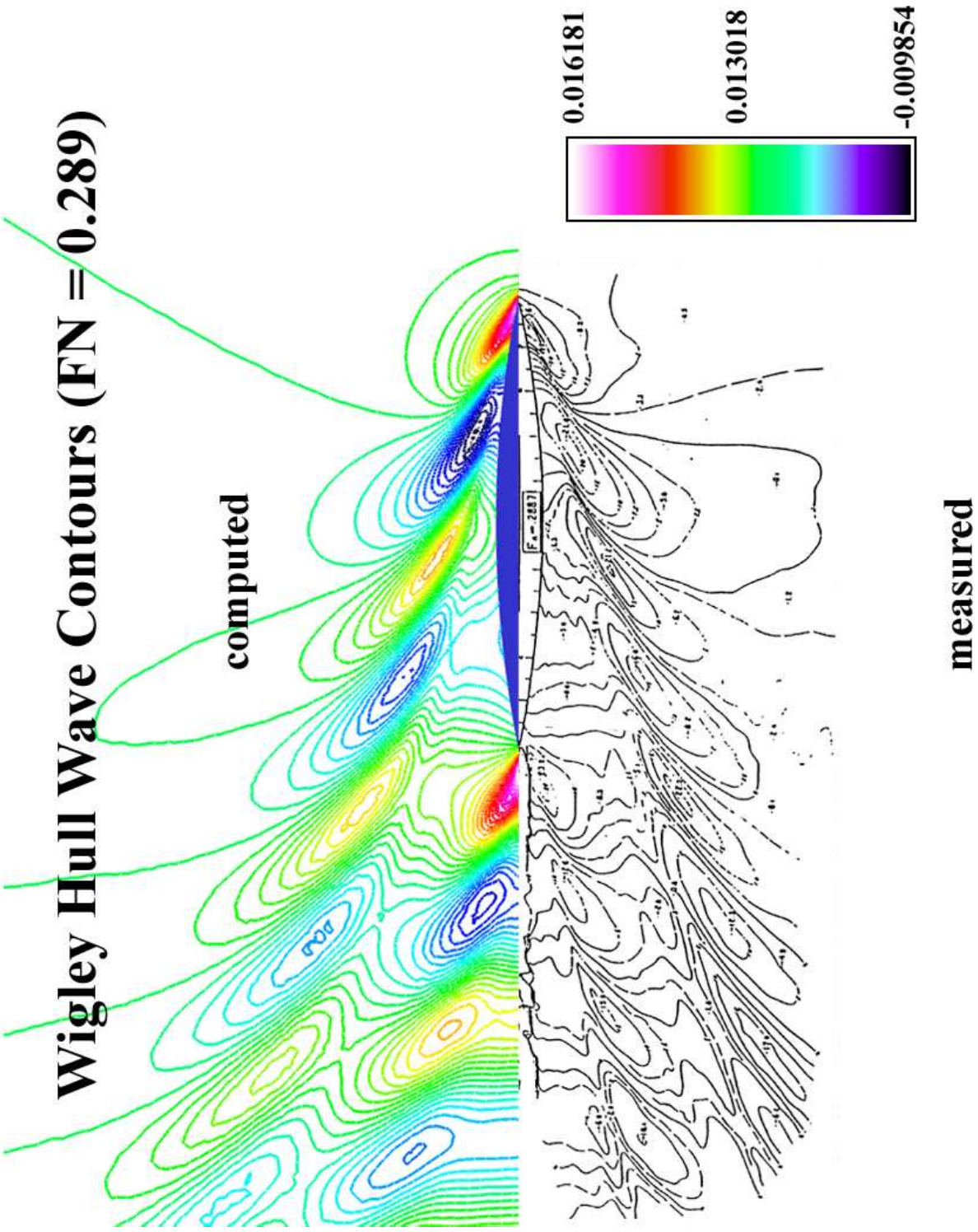

Figure 10: Comparison of Free Surface Elevations with Experiment at Fr = 0.289.

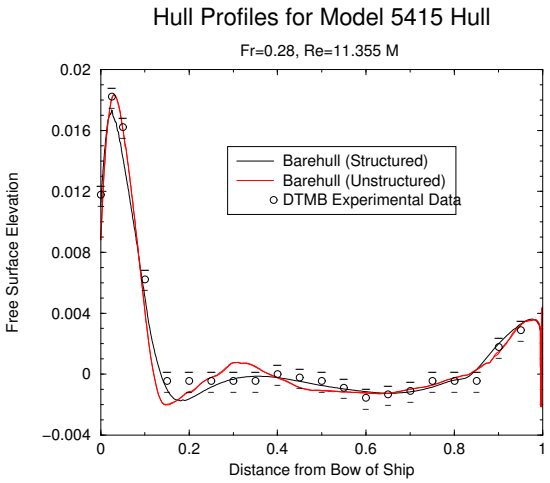

Figure 11: Nonappended 5415 Hull Profile

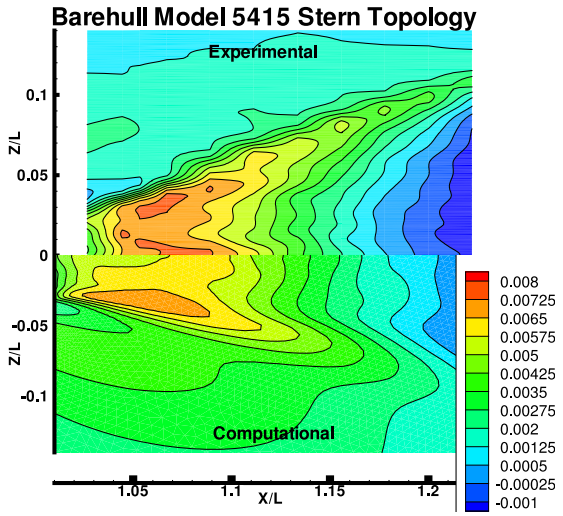

Figure 13: Stern Flow for DTMB Model 5415 Series

a Reynolds number of 11.655 million. Viscous spacing off of the hull was on the order of 10^{-6} which yielded y^+ values on the order of 1, indicating that the grid resolution near the hull was adequate for capturing the boundary layer details. The grid consisted of 1.88 million nodes, 3.73 million tetrahedra and 2.3 prisms, with 83292 nodes in the free surface, mostly packed near the hull.

Figure 12 shows the free surface contours around and behind the Model 5415 hull along with the underlying free surface grid, which fans out behind the stern. The free surface dissipates quite rapidly outside the regions of high resolution, and for each region of coarsening within the grid, the level of detail retained in the free surface decreases. The hull profile, shown in Figure 11, is compared against the experimental results and the results from the structured flow solver. Except for the region near $x = 0.2$, the hull profile matches the experimental data well and appears to reach the bow peak for the experimental results. Both the unstructured and structured results dip below the experimental results near $x = 0.2$ with the unstructured results differing more greatly. From simulations on other grids, it appears that the free surface in this region is not at a grid-independent level, meaning that the hull profile in this region is noticeably different when the grid spacing changes.

In the stern region, which is the region of the most difficulty for the numerical simulation due to the wetted transom stern, the agreement between the computational results and the experimental results are quite encouraging, as given in Figure 13. The discrepancies between the numerical and experimental are probably caused by the limited ability to capture viscous effects within the boundary layer adequately in this region and possibly by differences in the sink and trim between the experimental model and the numerical simulation. These issues will be studied in future simulations.

Conclusions

A robust, nonlinear free surface algorithm coupled with an incompressible Reynolds-Averaged Navier-Stokes solver on three-dimensional unstructured grids has been presented. The underlying unstructured solver has been developed to simulate turbulent boundary layer effects and is capable of performing rudder and propeller induced maneuvering. The addition of nonlinear free surface capabilities was a necessary step towards the simulation of maneuvering surface vessels.

The nonlinear free surface algorithm is an extension of the algorithm used in the structured code UNCLE developed by researchers at Mississippi State University. The kinematic free surface equation is solved at each time level, and the hydrostatic pressure is imposed on the Navier-Stokes solver via a characteristic variable boundary condition. After several iterations, the grid is moved to match the free surface while conforming to the underlying geometry, using a three-dimensional extension of the torsional spring method[15]. By allowing the grid to move, a nonlinear free surface solution is obtained.

In this paper, the implementation of the nonlinear free surface algorithm has been verified to demonstrate second-order convergence of the kinematic free

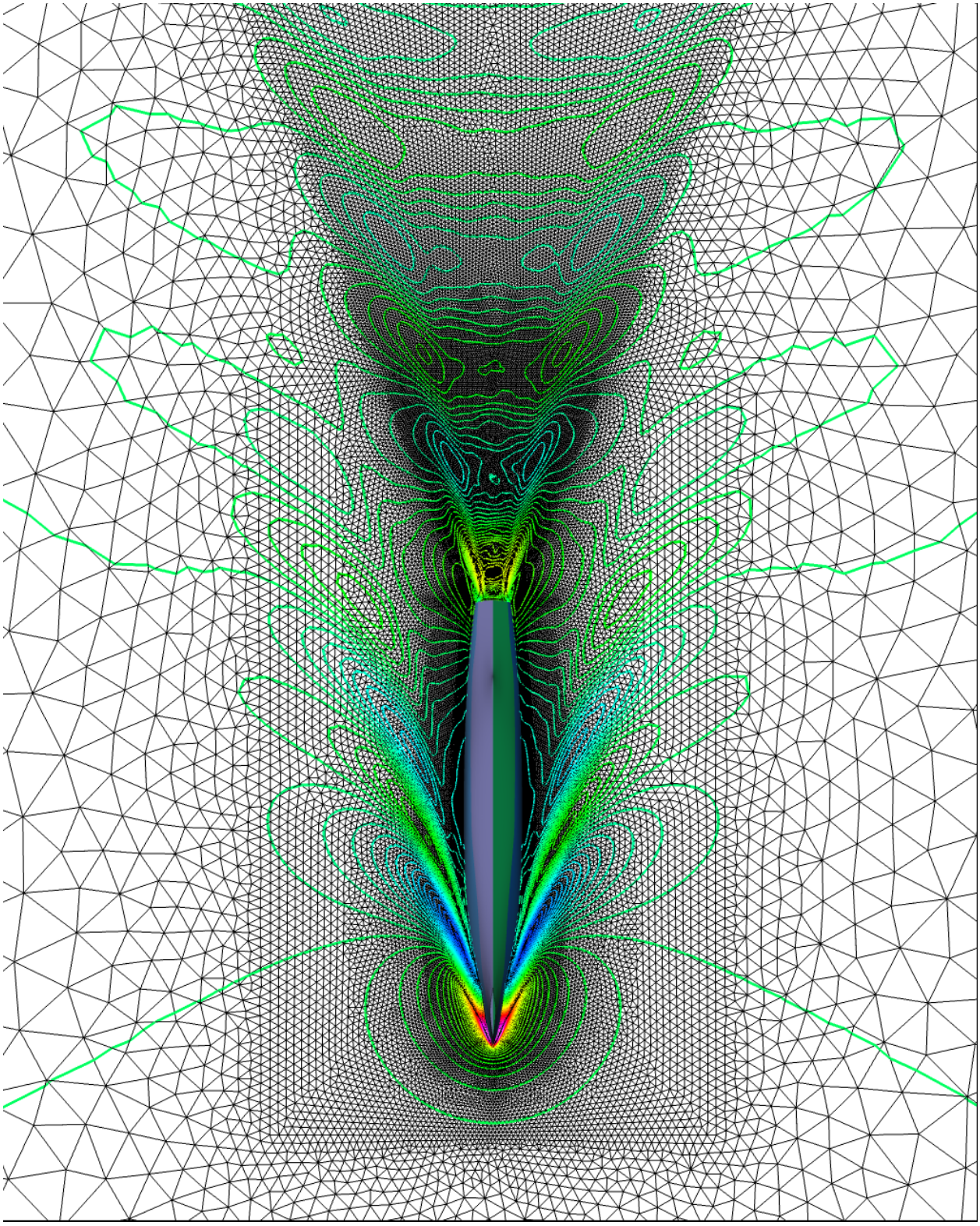

Figure 12: Free Surface Contours and Grid Resolution for 5415

surface equation solver on a circular free surface and superlinear convergence of free surface solver coupled with the RANS solver on a NACA 0012 hydrofoil. Furthermore, the verification study demonstrated that the grid movement algorithm did not degrade the overall order of accuracy of the coupled flow solver. The results of simulations involving viscous and inviscid Wigley hull and a nonappended DTMB Model 5415 Series hull showed excellent agreement with the available experimental data as well as numerical results produced by a more mature structured flow solver UNCLE. These studies indicate that free surface effects are maintained to the level of the grid refinement on the free surface, suggesting that the free surface effects can be simulated for several hull lengths downstream of the hull or submerged vessel. Finally, the flow around the DTMB Model 5415 Series hull in the transom stern region agrees quite well with the experimental data, demonstrating the ability of the code to simulate complicated free surface/viscous flow interactions.

Future work includes the study of the DTMB Model 5415 Series hull with its appendages and rotating propellers and the study of the effects of flow at angles of drift and through prescribed maneuvers on the free surface, in an ongoing effort to achieve the goal of rudder-induced, propeller driven surface vessel maneuvers.

Acknowledgments

This research was sponsored by the Office of Naval Research with Dr. L. Patrick Purtell grant monitor. This support is gratefully acknowledged. Special thanks to Toby Ratcliffe at Naval Surface Warfare Center Carderock Division for providing the data files for the experimental data and to Stephen Nichols at the Computational Simulation and Design Center for many hours of conversations about free surface issues, especially pertaining to the structured code UNCLE and to Dr. Lafayette Taylor, also at the Computational Simulation and Design Center for his encouragement and suggestions in this research effort.

References

[1] Daniel G. Hyams. *An Investigation of Parallel Implicit Solution Algorithms for Incompressible Flows on Unstructured Topologies*. PhD thesis, Mississippi State University, May 2000.

[2] D. L. Marcum. Unstructured Grid Generation Using Automatic Point Insertion and Local Reconnection. *The Handbook of Grid Generation*, p.18-1, 1998. edited by J.F. Thompson, B. Soni and N.P. Weatherill.

[3] M. Beddhu, L. K. Taylor, and D. L. Whitfield. A Time Accurate Calculation Procedure for Flows with a Free Surface Using a Modified Artificial Compressibility Formulation. *Applied Mathematics and Computation*, 65:33-48, 1994.

[4] M. Beddhu, M. Y. Jiang, L. K. Taylor, and D. L. Whitfield. Computation of Steady and Unsteady Flows with a Free Surface Around the Wigley Hull. *Applied Mathematics and Computation*, 89:67-84, 1998.

[5] M. Beddhu, M. Y. Jiang, D. L. Whitfield, L. K. Taylor, and A. Arabshahi. CFD Validation of the Free Surface Flow Around DTMB Model 5415 Using Reynolds Averaged Navier-Stokes Equations," *Proceedings of the Third Osaka Colloquium on Advanced CFD applications to Ship Flow and Hull Form Design*, 1998.

[6] M. Beddhu, S. Nichols, M. Y. Jiang, C. Sheng, D. L. Whitfield, and L. K. Taylor. Comparison of EFD and CFD Results of the Free Surface Flow Field about the Series 60 C_B = 0.6 Ship," *Proceedings of the Twenty-Fifth American Towing Tank Conference*, 1998.

[7] M. Beddhu, M. Y. Jiang, D. L. Whitfield and L. K. Taylor. Computation of the Wetted Transom Stern Flow over Model 5415." *Proceedings of the Seventh International Conference on Numerical Ship Hydrodynamics* Nantes, France, July 19-22, 1999.

[8] M. Beddhu, R. Pankajakshan, M. Y. Jiang, L. Taylor, M. G. Remotigue, W. R. Briley and D. L. Whitfield. Computation and Evaluation of CFD Results for Practical Ship Hull Forms. *Gothenburg 2000: A Workshop on Numerical Ship Hydrodynamics*, Gothenburg, Sweden, September 14-16, 2000.

[9] P. R. Spalart and S. R. Allmaras. A one-equation turbulence model for aerodynamic flows. *AIAA Paper 92-0439*, 1992.

[10] T. J. Coakley and T. Hsieh. A comparison between implicit and hybrid methods for the calculation of steady and unsteady inlet flows. *AIAA Paper 85-1125*, 1985. 21st AIAA/SAE/ASME/ASEE Joint Propulsion Conference, July 1985, Monterey, California.

[11] Alexandre Joel Chorin. A numerical method for solving incompressible viscous flow problems. *Journal of Computational Physics*, 2:12–26, 1967.

[12] Lafayette K. Taylor. *Unsteady Three-Dimensional Incompressible Algorithm based on Artificial Compressibility*. PhD thesis, Mississippi State University, 1991.

[13] D. G. Hyams, K. Sreenivas, C. Sheng, W. R. Briley, D. L. Marcum, and D. L. Whitfield. An investigation of parallel implicit solution algorithms for incompressible flows on multielement unstructured topologies. *AIAA Paper 2000-0271*, 2000. 38th AIAA Aerospace Sciences Meeting and Exhibit, January 2000, Reno, NV.

[14] D. G. Hyams, K. Sreenivas, K., C. Sheng, S. Nichols, L. K. Taylor, W. R. Briley, and D. L. Whitfield. An Unstructured Multielement Solution Algorithm for Complex Geometry Hydrodynamic Simulations. *Twenty-Third Symposium on Naval Hydrodynamics*, September, 2000. Falde Reuil, France.

[15] C. Farhat, C. Degand, B. Koobus, and M. Lesionne. Torsional Springs for Two-Dimensional Unstructured Fluid Meshes. *Computer methods in Applied Mechanics and Engineering* 163:231-245, 1998.

[16] John T. Batina. Unsteady Euler Airfoil Solutions Using Unstructured Dynamic Meshes *AIAA Paper 89-0115*, 1989. 27th AIAA Aerospace Sciences Meeting, January 1989, Reno, Nevada.

[17] K. P. Singh, J. C. Newman, and O. Baysal. Dynamic Unstructured Method for Flows Past Multiple Objects in Relative Motion. *AIAA Journal*, 33(4):641-649, April 1995.

[18] W. Kyle Anderson, and V. Venkatakrishnan. Aerodynamic Design Optimization on Unstructured Grids with a Continuous Adjoint Formulation. *AIAA Paper 97-0643*, 1997. 35th AIAA Aerospace Sciences Meeting and Exhibit, January 1997, Reno, NV.

[19] J. H. Duncan. The Breaking and NonBreaking Wave Resistance of a Two-Dimensional Hydrofoil. *Journal of Fluid Mechanics*, 126:507-520, 1983.

[20] T. Hino, L. Marinelli, and A. Jameson. A Finite-Volume Method with Unstructured Grid for Free Surface Flow Simulations *Proceedings: Sixth International Conference on Numerical Ship Hydrodynamics*, August, 1993. The University of Iowa, Iowa City.

[21] R. Löhner, C. Yang, and E. Onate. Viscous Free Surface Hydrodynamics Using Unstructured Grids. *Twenty-Second Symposium on Naval Hydrodynamics*, August, 1998. Washington, D.C.

[22] Lafayette K. Taylor, J.A. Busby, M. Y. Jiang, A. Arabshahi, K. Sreenivas, and D. L. Whitfield. Time accurate incompressible Navier-Stokes simulation of the flapping foil experiment. In *Sixth International Conference on Numerical Ship Hydrodynamics*, August 1993. Iowa City, Iowa.

[23] *Cooperative Experiments on Wigley Parabolic Models in Japan*' Nineteenth R. C. Report International Towing Tank Conference (ITTC), 1983.

[24] T. J. Ratcliffe, and W. T. Lindenmuth. Kelvin Wake Measurements Obtained for Five Surface Ship Models. DTRC-89/038, January, 1990.

[25] T. J. Ratcliffe. An Experimental and Computational Study of the Effects of Propulsion on the Free-Surface Flow Astern of Model 5415. *Twenty-third Symposium on Naval Hydrodynamics*, Spetember 2000. Falde Reuil, France.

[26] http://www.iihr.uiowa.edu/gothenburg2000/5415/combatant.html.